

# VALIDATION OF MULTIPHASE FLOW SIMULATIONS BY EXPERIMENTAL MEASUREMENTS IN A CHANNEL FLOW

Marwan Khaled<sup>1\*</sup>, Benedikt Faraji-Tajrishi<sup>1</sup>, Arnold Herrgen<sup>2</sup> & Bernhard Weigand<sup>1</sup>

<sup>1</sup>Institute of Aerospace Thermodynamics (ITLR), University of Stuttgart, Stuttgart, Germany <sup>2</sup>MTU Aero Engines AG, Dachauer Str. 665, 80995 Munich, Germany <sup>\*</sup>Corresponding author: marwan.khaled@itlr.uni-stuttgart.de

#### **Abstract**

In order to mitigate the impact of aviation on climate change, several new concepts are investigated today. One of them is the Water-Enhanced Turbofan concept (WET) [1], where the separation process of water from the exhaust gas flow is of great importance. Depositing water droplets on the walls form a wall-film which can be separated from the gas flow, e.g. through the use of separation lips. To enhance our understanding of the water separation process, experiments are performed in a rectangular channel under various conditions. Additionally, Computational Fluid Dynamics (CFD) simulations are carried out using the commercial STAR-CCM+ software. The primary objective of this study is to develop a numerical model and to validate it against experimental data. To achieve this, Euler-Lagrange simulations combined with a fluid film model are conducted. Numerical results for the static pressure and the amount of separated water show good agreement with experimentally measured data. Additionally, the fluid film model and the corresponding sub-models are observed.

Keywords: Multiphase Flow, Water Separation, Euler-Lagrange, Fluid Film

#### 1. Introduction

Since the deployment of the first gas turbine-powered commercial jet airliner about 70 years ago, civil aviation has undergone enormous technological advancements. However, air traffic emissions contribute to anthropological climate change by approximately 5% [2]. Therefore, sustainability plays a major role in the development of future aero engines. Researchers all over the world have proposed new concepts and technologies to reduce the impact of aviation on climate change. One such concept is the Water-Enhanced Turbofan (WET) [1], which has been proposed by MTU Aero Engines. According to Kaiser et al. [1], the WET concept will lead to an increased specific power output and to significant improvements in thermodynamic efficiency compared to conventional turbofans. Additionally, it will reduce the climate-relevant contrails and emissions, namely CO2 and NOx. It is a novel dual-fluid propulsion system for aircraft and it is based on the Cheng Cycle [3], featuring the injection of superheated steam into the combustion chamber. The WET concept requires a semi-closed water cycle. Thus, the separation process of water from the exhaust flow is of great importance. To obtain water for the cycle, which is injected into the combustor, water must be recovered from the exhaust gas flow through a condenser and a subsequent Water-Recovery-Unit (WRU). At the University of Stuttgart in the Institute of Aerospace Thermodynamics (ITLR), the basic physics of the water separation process are being investigated in more detail performing experiments and numerical multiphase flow simulations in a channel flow operated with supersaturated air and liquid water. The primary goal is to achieve a deeper understanding of the water separation process and to enhance the efficiency of the WRU. First, the experimental test rig is described, followed by an outline of the numerical setup. Subsequently, results of the single-phase flow and a spray nozzle show good agreement with the experimental data. Furthermore, experiments and multiphase flow simulations are conducted for the supersaturated channel flow. This study primarily focuses on numerical investigations, which demonstrate comparable results to experimental data.

#### 2. Experimental Setup

The experimental test rig consists of several parts: an evaporator, a humidifier, a convergent nozzle, a test section and an outlet, as shown in Figure 1 (a). To maintain flexibility, the different parts of the channel are connected through flanges. The evaporator is employed to attain a fully saturated airflow

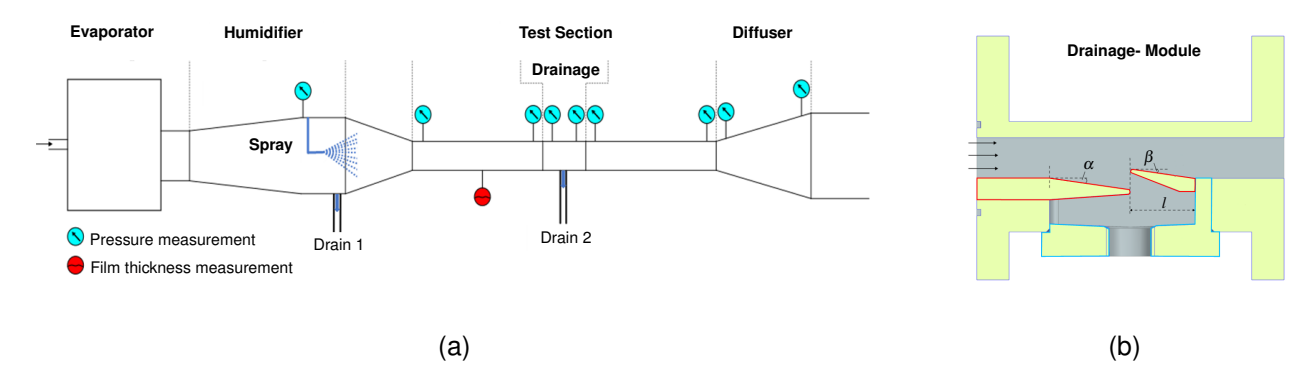


Figure 1 – Schematic view of the experimental test rig (a) and the design of the drainage module (b).

at the entrance of the humidifier. Within the humidifier, which has a circular cross-section, a spray nozzle injects water droplets into the airflow, inducing a supersaturated flow. Thus, a multiphase flow is created, and different operating points are provided. Subsequently, a convergent nozzle accelerates the flow to achieve the desired conditions at the inlet of the test section. The cross- section of the channel changes from circular to rectangular. Air flow Mach numbers up to  $\mathrm{Ma}=0.3$  are realized. The Mach number of the airflow is defined by

$$Ma = \frac{u}{u_s}.$$
 (1)

Where u is the mean axial velocity of the airflow and  $u_s$  is the speed of sound. The air is assumed to follow the state equation for an ideal gas model, leading to  $u_s = \sqrt{\kappa RT}$  with  $\kappa$  being the isentropic exponent, R the ideal gas constant and T the static temperature. Additionally, the airflow Reynolds number is defined using the hydraulic diameter  $D_h$  of the the test section

$$Re = \frac{\rho u D_h}{\mu}.$$
 (2)

Here,  $\rho$  is the density and  $\mu$  the dynamic viscosity of the air. Within the test section, a drainage module is employed to separate water from the airflow. To investigate the impact of the geometry on the separation process, a variable configuration is utilized for the separation lips, as shown in Figure 1 (b). Except for the convergent nozzle, the entire channel is made out of perspex to facilitate optical measurements. A confocal chromatic sensor from Keyence is implemented at the bottom wall of the test section to measure the film thickness. Confocal chromatic imaging (CCI) measures film thickness by analyzing the shift in focal position across different wavelengths of light, exploiting chromatic aberration. This allows for precise determination of the thickness of thin films with high accuracy and resolution. The CCI-sensor has a measurement accuracy of  $\pm 0.25\,\mu m$ . The measurement of the film thickness takes 3 to 5 seconds at a sampling rate of  $1\,\mathrm{kHz}$ . The film thickness is then time-averaged. As shown in Figure 1 (a), static pressure measurements are conducted at various distances along the channel to provide comprehensive data for analysis. The used sensors from Scanivalve have a measurement accuracy of  $\pm 30\,\mathrm{Pa}$ . The pressure is measured for 120 seconds at a sampling rate of  $1\,\mathrm{Hz}$ . To enhance the evaluation, two sensors are employed for each measurement point before performing time-averaging.

Two scales are used to gauge the mass flow rates of the separated water through drain 1 ( $\dot{m}_{\rm w,DR1}$ ) and drain 2 ( $\dot{m}_{\rm w,DR2}$ ), respectively. For this experiment, only the water separation on the bottom of the channel is considered. In order to evaluate the total separation efficiency of the WRU, water separation on the other walls should be taken into account, too. However, this test rig is primarily used for the development of experimental measurement methods and the validation of numerical models.

#### 3. Numerical Setup

The main features of the experimental test rig (cf. Figure 1 (a)) are used to build the simulation domain for numerical analyses. Unsteady multiphase Computational Fluid Dynamics (CFD) simulations are carried out using the commercial STAR-CCM+ software (version 18.06).

#### Single-phase Flow

Initially, steady-state single-phase flow simulations are performed for dry air to verify the boundary conditions. Within this approach, the airflow is modeled as continuum for which the governing mass, momentum and energy equations are solved. The turbulent airflow is modeled using the Reynolds Averaged Navier-Stokes equations (RANS). Turbulence is described by the LAG Elliptic Blending k- $\varepsilon$  turbulence model [4] in combination with wall functions. Furthermore, airflow is treated as an ideal gas.

## Multiphase Flow

The solution of the single-phase flow is then used as an initial state for the unsteady multiphase flow simulation, employing a two-way coupled Euler-Lagrange approach. This allows the phases to exchange mass, momentum and energy through source and sink terms in the governing equations. For more details, the reader is referred to STAR-CCM+ User Guide [5]. The injected droplets are modeled as spherical Lagrangian particles using a parcel concept. To satisfy the statistics of the droplet distribution and in order to reduce the simulation time, different parcel streams are used. The equations of motion for each parcel are solved in Lagrangian approach to calculate their trajectories. Two ordinary differential equations are necessary to calculate the trajectory of a single parcel. The positions  $\vec{x}_p$  and the velocities of the parcel  $\vec{u}_p$  are solved by

$$\frac{d\vec{x}_{\rm p}}{dt} = \vec{u}_{\rm p},\tag{3}$$

$$m_{\rm p}\frac{d\vec{u}_{\rm p}}{dt} = \sum \vec{F}_{i}.\tag{4}$$

Here,  $m_{\rm p}$  is the parcel mass and  $\vec{F}_i$  devote the acting forces. The drag force, gravitational force and turbulent dispersion are considered. The Schiller-Naumann correlation [6] is accounted to calculate the drag force. The turbulent dispersion considers the impact of a particle in turbulent flow experiencing a randomly varying velocity field, to which it reacts based on its inertia. This phenomenon is represented by a stochastic approach that incorporates the influence of instantaneous velocity fluctuations on the particle [5]. As given by Sommerfeld et al. [7], the virtual mass force, the pressure gradient force and the Basset force can be neglected for gas-liquid flow since  $\rho_g/\rho_l << 1$ .

In the experiments a thin water film appears at the walls. In STAR-CCM+ [5] a fluid film model is implemented which is valid for thin films. Hence, the water film is modeled as a thin, two dimensional laminar fluid film. This means, that the wall-normal profiles of velocity and temperature are obtained from boundary-layer approximations. It assumes a piece-wise linear profile for temperature and a parabolic velocity profile. The fluid film equations are solved on a two dimensional shell mesh on which the fluid film is allowed to form. This allows a simplified solution procedure for the film flow. The continuity

$$\frac{\partial \rho_{\text{Film}} \delta_{\text{Film}}}{\partial t} + \nabla \cdot [\rho_{\text{Film}} \delta_{\text{Film}} u_{\text{Film}}] = S_u$$
 (5)

is solved for the film thickness  $\delta_{Film}$ , and the momentum equation

$$\frac{\partial (\rho_{\text{Film}} \delta_{\text{Film}} u_{\text{Film}})}{\partial t} + \nabla \cdot \left[ (\rho_{\text{Film}} \delta_{\text{Film}} u_{\text{Film}}) u_{\text{Film}} \right] = -\nabla p_{\text{Film}} + \nabla \cdot \tau_{\text{Film}} + \rho_{\text{Film}} g + S_m + f_v$$
 (6)

is solved for the average velocity of the film  $u_{\rm film}$ . Since the water film is assumed to be incompressible, the density of the film is set to a constant value  $\rho_{\rm film}={\rm const.}$ . The quantity  $S_u$  in Equation 5 represents the mass source or sink, contributing to phenomena such as droplet impingement, film stripping, and mass transfer. In this context, the momentum source  $S_m$  in Equation 6 corresponds

to the mass source  $S_u$ . The pressure-based and stress-based forces are represented by the terms  $\nabla p$  and  $\nabla \cdot \tau$ , respectively. Further, the gravity force  $\rho_{\mathrm{Film}}g$  is considered. The quantity  $f_v$  represents volume forces. At the fluid film-gas interface, surface tension results from fluid molecules attraction, leading to an inward force. Following Meredith et al. [8] this force

$$f_{\sigma} = p_{\sigma} n + \tau_{\sigma} \tag{7}$$

can be divided into normal and tangential components. Here,  $p_{\sigma}$  is the capillary pressure and  $\tau_{\sigma}$  is the contact line force. In STAR-CCM+ this contact line force is calculated as

$$\tau_{\sigma} = b\sigma(1 - \cos(\theta))\nabla w. \tag{8}$$

Here, b is an empirical parameter to calibrate the model, w is defined as 1 for film thickness values above a specified value and 0 elsewhere. Further, the contact angle  $\theta$  between the film and the wall is important for the wetting behavior of the film. By default a static contact angle is used. For a moving film this is not valid. Therefore, the dynamic contact angle model by Kistler [9]

$$\theta_d = f_{\text{Hoff}}(Ca + f_{\text{Hoff}}^{-1}(\theta_s)) \tag{9}$$

was implemented as a field-function. Here,  $Ca = \mu_{\text{Film}} u_{\text{Film}} / \sigma$  is the film Capillary number,  $f_{\text{Hoff}}$ 

$$f_{\text{Hoff}}(\theta_s) = \arccos\left[1 - 2\tanh\left(5.16\left(\frac{\theta_s}{1 + 1.31\theta_s^{0.99}}\right)^{0.706}\right)\right].$$
 (10)

represents the Hoffmann-function and  $\theta_s$  is the static contact angle. In order to solve analytically the inverse function  $f_{\rm Hoff}^{-1}$ , the exponent in the term  $\theta_s^{0.99}$  is set to 1. The static contact angle for water and perspex is measured to  $\theta_s = 81^{\circ}$ .

Further models are required to account for the interaction between the Lagrangian-phase and the fluid film model. These interactions include the mass and momentum transfers between the phases. The Bai-Gosmann [10] model is applied to account for the interaction between droplets and walls, as well as droplets and the film. The occurrence of various wall/film impingement modes (such as adhesion, rebound, spreading, and splashing) depends on the incident droplet Weber number, which is defined as

$$We = \frac{\rho_p v_{p,n} D_p}{\sigma_p}.$$
 (11)

Here,  $v_{p,n}$  is the vertical, surface-normal velocity of the impinging droplet. Droplets which are impinging onto a wall associated to the shell region contribute to the formation of a fluid film. Furthermore, experimental images show that water droplets are ejected from the film into the core flow. These phenomenon can be attributed to aerodynamic instabilities within the film, necessitating the incorporation of additional sub-models. In STAR-CCM+ [5], two stripping models are available to consider this phenomenon, namely wave stripping and edge stripping. These models are based on the works of Maroteaux et al. [11] and Friedrich et al. [12]. Wave stripping accounts the ejection of droplets from the film surface due to the growth of the most unstable disturbances. The separation of the film at a sharp corner is considered through edge stripping. According to Friedrich et al. [12] film separates at a sharp corner when film inertia overcomes the surface tension and gravitational effects. For the simplicity, only wave stripping is considered in this work. For the setup depicted in Figure 2, a stagnation inlet and a mass flow outlet boundary condition are applied to the humidifier inlet and at the diffuser outlet, respectively. The used values are taken from the experiments. Moreover, the spray nozzle is represented as a solid cone injector with a specified droplet size distribution, droplet velocity, cone angle, mass flow rate, obtained from experimental investigations of the spray nozzle. The mesh for the numerical analyses is generated directly in the STAR-CCM+ package and contains unstructured polyhedral cells with local refinements at drainage inlet, as shown in Figure 2. Two prism layers in combination with wall functions are applied to account for the boundary layer flow. These settings lead to a total number of 298,474 cells for the test rig. The fluid film shell regions contain

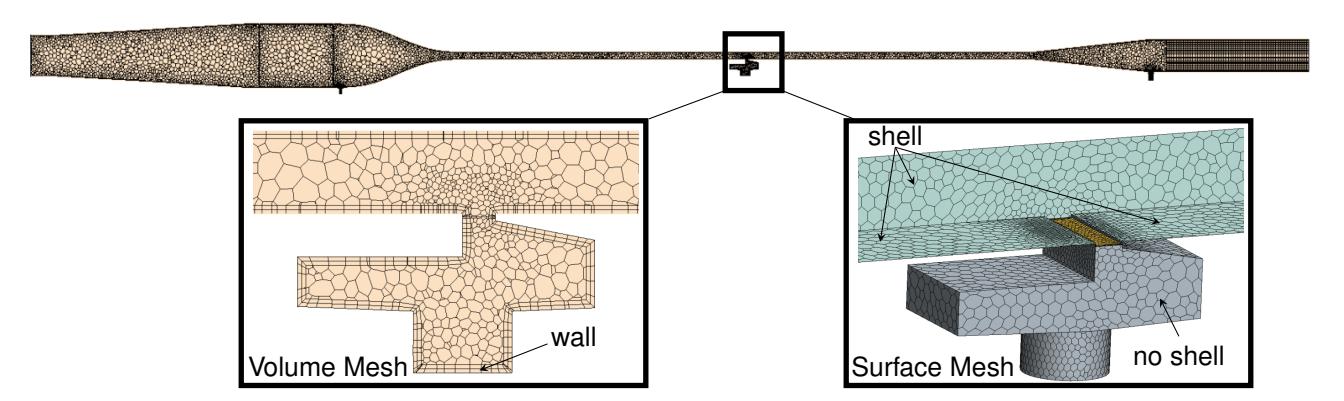


Figure 2 – Computational mesh considered in the CFD simulations.

59,478 cells overall. As shown in the detailed views in Figure 2, only the green-colored regions are counted as shell regions. To avoid nonphysical behavior in the fluid film model, the drainage itself is not considered as a shell region. Additionally, the bottom edge of the drainage inlet is assumed as an outlet for the fluid film, with any droplets entering the drainage considered to exit the domain. This procedure simplifies the evaluation of the separated mass flow and no edge stripping is required at the drainage inlet. Finally, the three dimensional unsteady RANS equations with all considered models and boundary conditions are applied to the numerical domain. For the unsteady simulation runs, a time step of 5.0E-4s (5 inner iterations per time step) is considered to accurately capture physical phenomena and to ensure a stable simulation run. Every simulation was run until the characteristic quantities, such as pressure, drain mass flow rates, and film thickness, converged to near steady-state values.

## 4. Results and Analyses

In this section, preliminary results from experimental measurements and CFD simulations are compared and analyzed. All presented results are time-averaged until near by steady-state is achieved. Initially, 3D-RANS simulations are conducted for the dry airflow to evaluate the pressure losses of various drainage designs. Subsequently, the boundary conditions for the spray nozzle are validated using experimental data. Finally, unsteady multiphase flow simulations are performed. The used geometry for the numerical domain differs slightly from the real application. Additionally, a flexible hose is used at the outlet to remove the remaining water from the system, which is not resolved in the numerical domain.

#### 4.1 Single-Phase Flow

Initially, measurements and numerical simulations for the dry airflow are performed. In this study, three different drainage configurations were tested and simulated for two distinct operating points: Ma = 0.2 and Ma = 0.3. Additionally, during the experiments, the drainage lids were closed to prevent mass flow losses. Therefore, a wall boundary condition is applied for the drainage, as shown in Figure 2. For the case Ma = 0.2, Figure 3 shows the numerically obtained results for the normalized static pressure along the channel length, compared with experimental data. The pressure distribution along the channel length is well predicted for all configurations, with a maximum deviation below 1% between numerical and experimental results. Slightly higher deviations between numerical and experimental results occur for configuration 3, compared to configurations 1 and 2. One reason for that is the flow separation at the inclined downstream lip in configuration 3, which is not completely captured by the used wall functions. For all configurations two prism layers in combination with wall functions are applied to account for the boundary layer flow. STAR-CCM+ uses a modified description for the wall functions [5]. These wall functions were originally developed for the simple case of a flow over a flat plate. However, the wall functions underestimate the effect of flow separation and can lead to higher deviations between numerical and experimental results. To ensure optimal performance, it is crucial to minimize pressure losses in the WRU. In this regard, pressure losses across the drainage module are evaluated for the three configurations in Figure 4, providing insight into the effectiveness



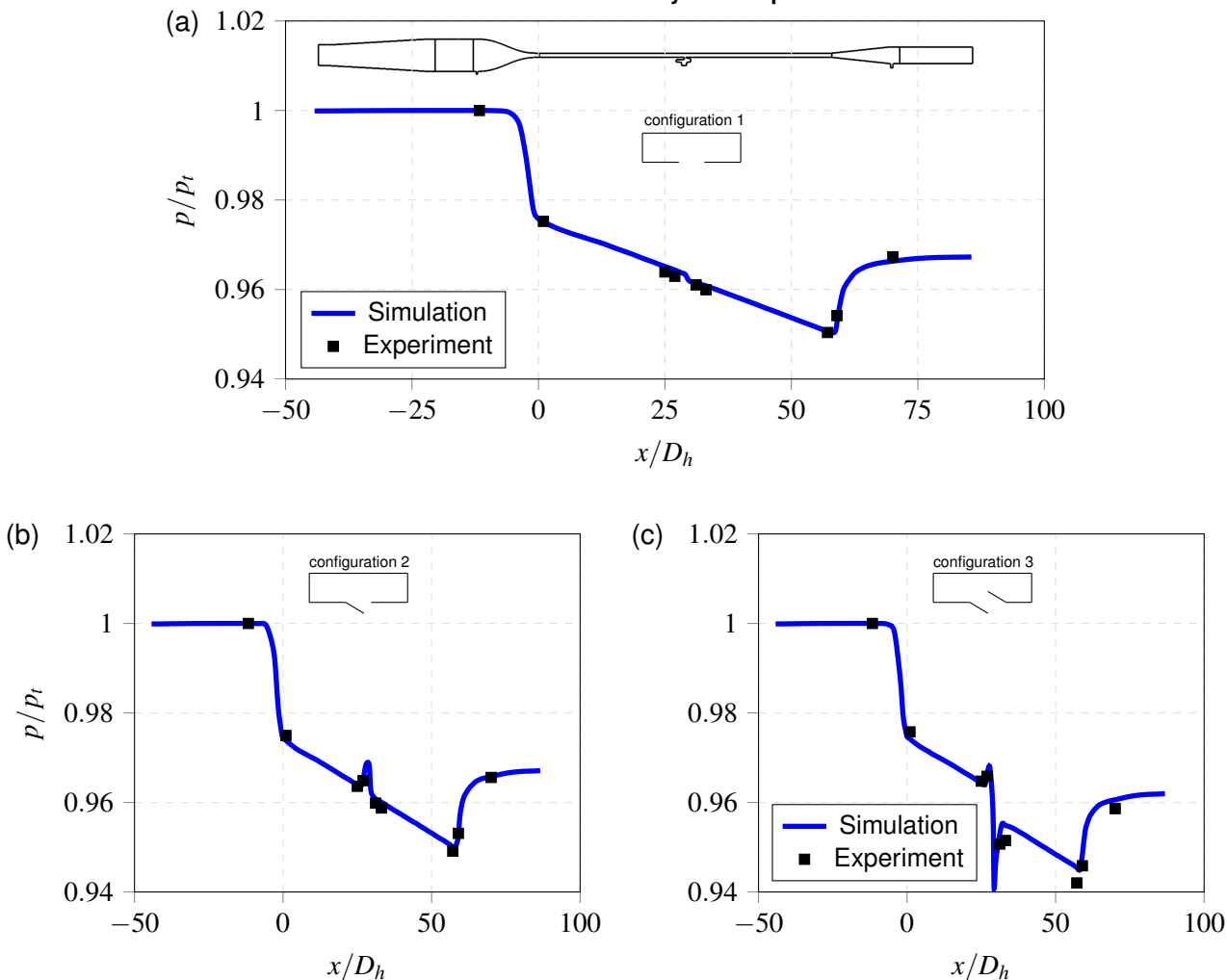


Figure 3 – Comparison between simulated and measured pressure distributions along the channel length for the configuration 1 (a), configuration 2 (b), configuration 3 (c) and a Ma = 0.2.

of various separation lip designs. The pressure losses are nondimensionalized by the absolute total pressure. The pressure losses increase with the inclination angle of the separation lips, due to flow separation. Furthermore, the pressure losses increase for all three configurations as the Mach number rises from Ma = 0.2 (Figure 4 (a)) to Ma = 0.3 (Figure 4 (b)).

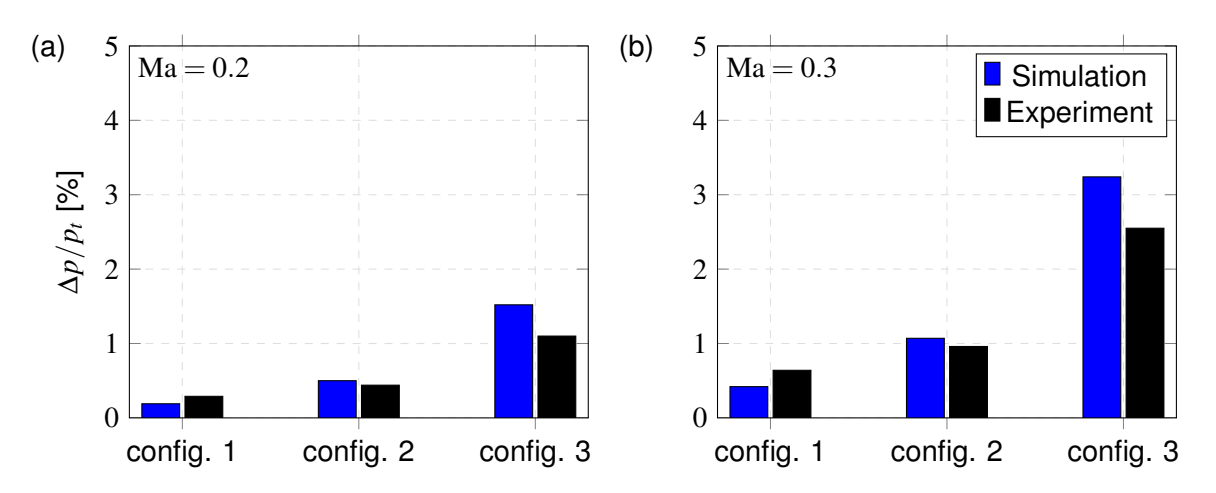


Figure 4 – Comparison of the simulated and measured pressure losses across the drainage module for three configurations at Mach numbers Ma = 0.2 (a) and Ma = 0.3 (b).

# 4.2 Multiphase Flow Spray- Validation

In the experimental test rig a spray nozzle injects water droplets into the airflow, inducing a supersaturated flow. To accurately simulate the multiphase flow, a valid boundary condition is necessary to model the injected water droplets. Modeling and measuring the spray nozzle are inherently complex tasks that require detailed analysis. In preliminary in-house work, droplet size and velocity distributions of different hollow cone injectors were measured using Phase Doppler Anemometry (PDA). Figure 5 (a) shows a schematic view of the experimental setup. The measurements were performed under atmospheric conditions, thus, not in the channel flow. The spherical droplet diameters and the velocities of the droplets were measured in two different measurement sections (MS1, MS2) and at different radial positions. The data from this experimental work are used to build a numerical model for the spray. An unstructured mesh with local refinements is used for the numerical domain, as illustrated in Figure 5 (b). Unsteady three dimensional Euler-Lagrange simulations are conducted. Two-way coupling, the drag force and turbulent dispersion are considered for the droplets. Atmospheric pressure is applied to all boundaries. In this work, a solid cone injector model within STAR-CCM+

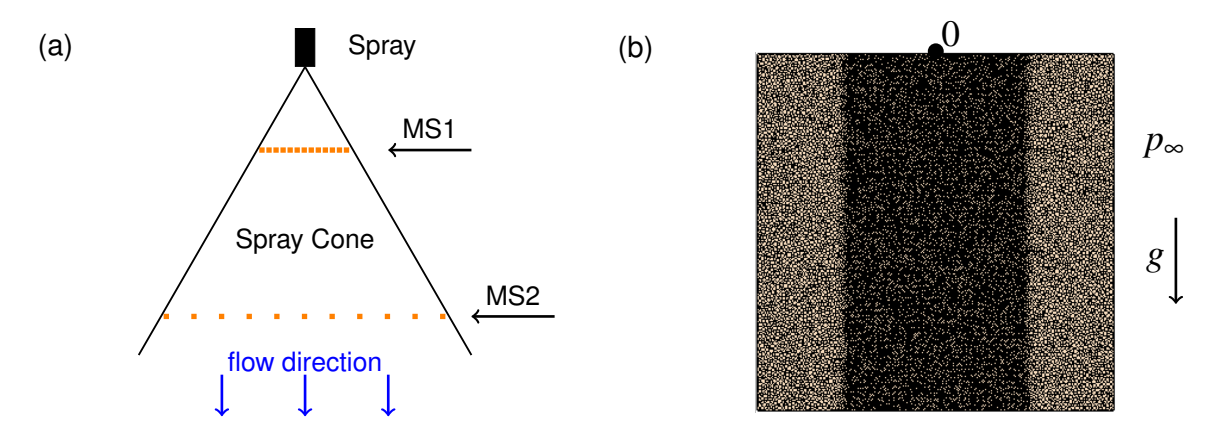


Figure 5 – Schematic view of spray measurements (a) and numerical mesh for spray validation (b)

is employed to validate the droplet diameters and velocities against experimental data. A cumulative density function (CDF), obtained from experimental data in MS1, is applied at the inlet of the injector for the droplet size distribution. Additionally a droplet mass flow  $\dot{m}_{\rm inj}/\dot{m}\approx 0.33$  is used, which is taken from the experiment. Furthermore, the droplet velocity needs to be specified. According to Badra et al. [13], the magnitude velocity of a hollow cone spray nozzle can be calculated using the following correlation

$$|u_{\rm inj}| = C_D \sqrt{\frac{2\triangle p}{\rho_1}}.$$
 (12)

Here, the quantity  $C_D=0.7$  is an empirical parameter,  $\Delta p$  is the operating pressure difference of the nozzle and  $\rho_l$  is the density of the water droplet. In order to calculate the velocity vector of the injected droplets, a specified spray angle is required. The spray angle was set to  $\varphi \approx 60^\circ$  in accordance with experimental results.

Figure 6 presents a comparison between numerically calculated results and experimental data. Specifically, Figures 6 (a) and (b) depict the dimensionless mean droplet diameter, while Figures 6 (c) and (d) show the dimensionless mean droplet velocity distributions in MS1 and MS2, respectively. Smaller droplets tend to concentrate in the center of the spray and exhibit higher velocities compared to larger droplets, which are found at the spray periphery. Due to their larger cross-sectional area, larger droplets experience greater absolute drag forces, causing them to decelerate and move toward the spray periphery. It is evident that the spray angle has a significant effect on the calculated distributions. In reality, the disintegration of a jet results in a spray formation, a process that is highly complex and cannot be fully captured by the chosen Euler-Lagrange approach. Near the injector inlet, higher shear forces act on the jet, resulting in increased drag and leading to a higher spray

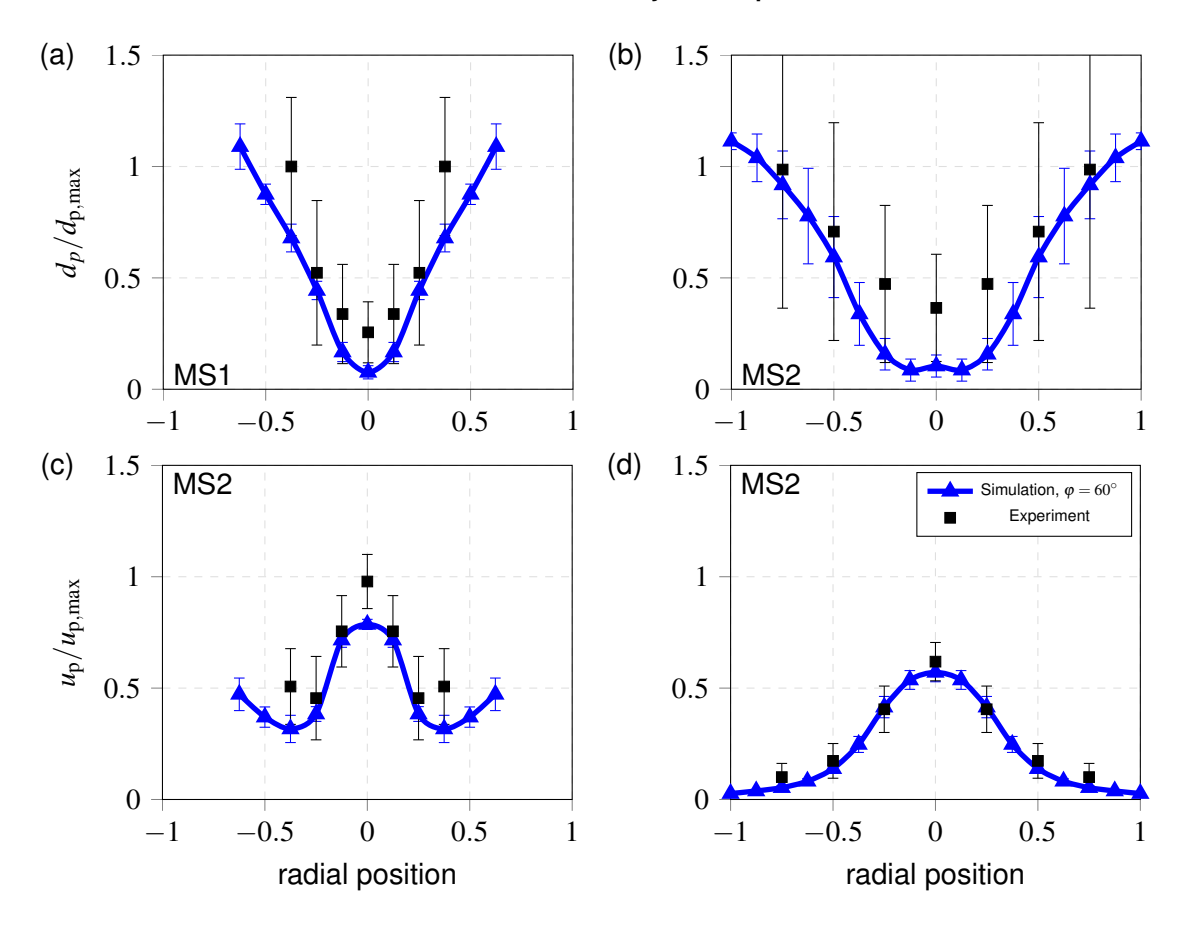


Figure 6 – Radial droplet diameter and velocity distributions in MS1 (left) and MS2 (right), respectively.

angle. To accurately capture this effect, consideration of a slightly higher spray angle is necessary in the simulation. Hence, a spray angle of  $\varphi=60^\circ$  is chosen, compared to  $\varphi_{\rm exp}\approx54^\circ$  from experimental results. Furthermore, the standard deviation for both simulation and experimental data is shown in Figure 6. The experiment data show higher scattering compared to the numerical data. Moreover, the experimental data are obtained from point measurements while the numerically data are evaluated on ring segments for different radial positions. An overall good agreement is achieved for both the diameter and the velocity distribution. Since the spray nozzle is now validated, the boundary condition for the channel flow can now be specified.

## Channel Flow

The results and findings obtained from the steady single-phase flow and unsteady spray simulations are used for the multiphase flow simulation. Experiments showed that the reference geometry of the drainage leads to lower pressure losses at similar values for the amount of separated water, compared to configurations 2 and 3. Therefore, only the reference geometry (configuration 1) is investigated numerically. The data from this experimental work are used to built a numerical model for the spray. All models and settings from section 3 are considered for this study, except for the stripping models. In this section, the pressure losses, the film thickness and the the amount of separated water are compared for the experiment and the simulation.

Figure 7 shows for the multiphase flow the dimensionless velocity field compared to the single-phase flow. The velocity is nondimenionalized by the mean velocity at the inlet of the test section. Hereby, the effect of the injected droplets on the air velocity can be observed in the humidifier. The injected droplets have significantly higher velocities than the airflow in the humidifier. This leads to an acceleration of the airflow in the core of the spray compared to the single-phase flow simulation. Furthermore, large areas of recirculation appear in the outer regions of the humidifier and the nozzle,

resulting in higher back pressures. Consequently, a higher total pressure value at the inlet is required for the multiphase flow compared to the single-phase flow. While the velocity field in the test section is similar, it differs from that of the single-phase flow at the inlet of the diffuser. The simulated and

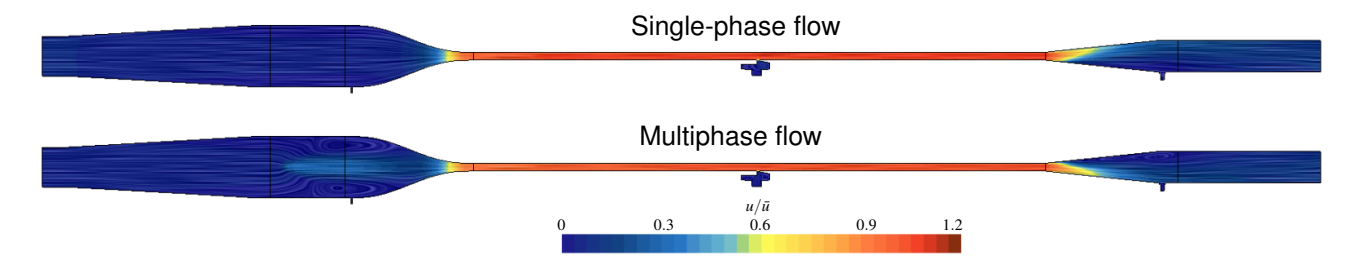


Figure 7 – Velocity field comparison between single-phase and multiphase flow simulation.

measured pressure changes across different parts of the test rig are illustrated in Figure 8. These pressure changes are nondimensionalized by the absolute total pressure at the inlet of the humidifier. Additionally, experimental data for pressure changes from the single-phase flow are shown as reference data. It can be observed that pressure changes are higher in the multiphase flow compared to the single-phase flow in almost every part of the test rig. Due to the use of two-way coupling, the dispersed phase (droplets) can have a significant effect on the continuous phase (air). Specifically, in

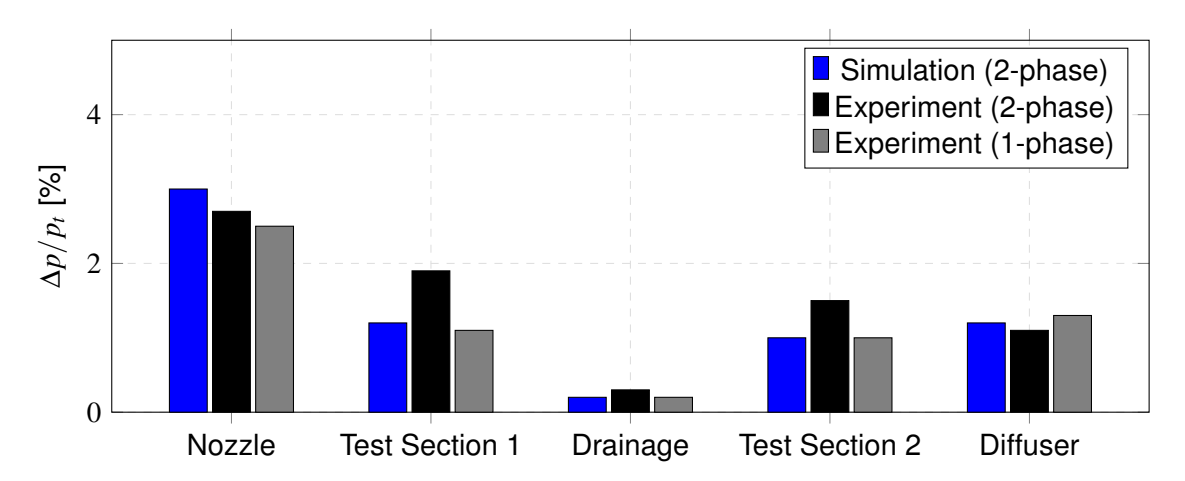


Figure 8 – Comparison of the simulated and measured pressure losses across different parts.

the nozzle, high-velocity droplets further accelerate the airflow (Figure 7), resulting in higher pressure changes compared to the single-phase flow. Nevertheless, pressure changes are dominated by the single-phase flow, especially in the test section. Good agreement is achieved between simulation and experiment for all parts, with a maximum deviation below 1%.

In the experiment, a thin water film forms due to droplet-wall interactions. Therefore, the fluid film model is applied to the channel walls in the simulation domain. The governing equations are solved for the fluid film on two-dimensional shell regions, as described in section 3. In Figure 9, the dimensionless fluid film thickness is shown for the bottom and a side wall of the test section. Additionally, the particles are displayed to show the annular mist flow. For the drainage itself, no shell region is considered. Therefore, no film occurs on the walls of the drainage. Consequently, a film-outlet boundary condition is imposed at the edge of the drainage inlet to avoid the usage of the edge stripping model, which requires further validation. It is expected that a thicker film forms at the bottom of the test section, because more droplets impact the bottom due to gravity. The fluid film thickness increases downstream nearly linear until it reaches the drainage, where it is removed from the domain at the drainage inlet. Downstream of the drainage, a new film is created on the bottom of the test section due to further droplet-wall interactions. This is shown in Figure 10 (a). The dimensionless film thickness is shown at the centerline of the bottom wall across the dimensionless channel length

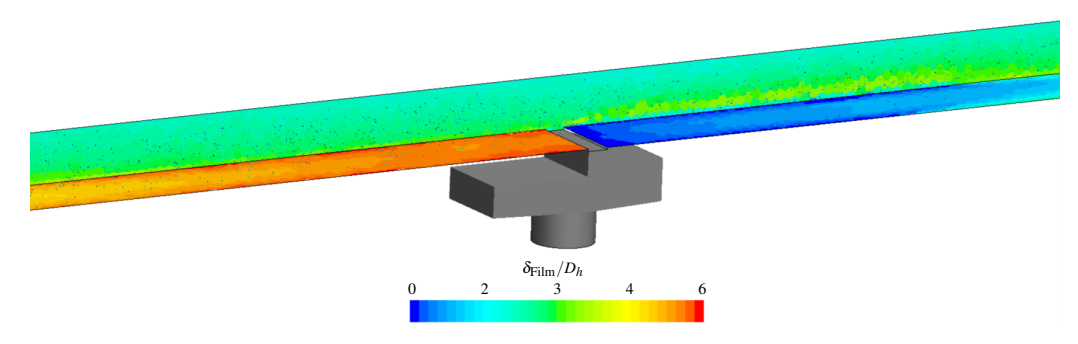


Figure 9 – Dimensionless fluid film thickness on the walls of the test section.

and compared with experimentally measured film thickness. Moreover, as shown in Figure 10 (b), the film distribution across the channel width appears consistent and physically plausible, with higher film thickness values observed in the corners of the rectangular channel. A slightly asymmetrical behavior is observed. However, a significant deviation is observed between experimentally measured

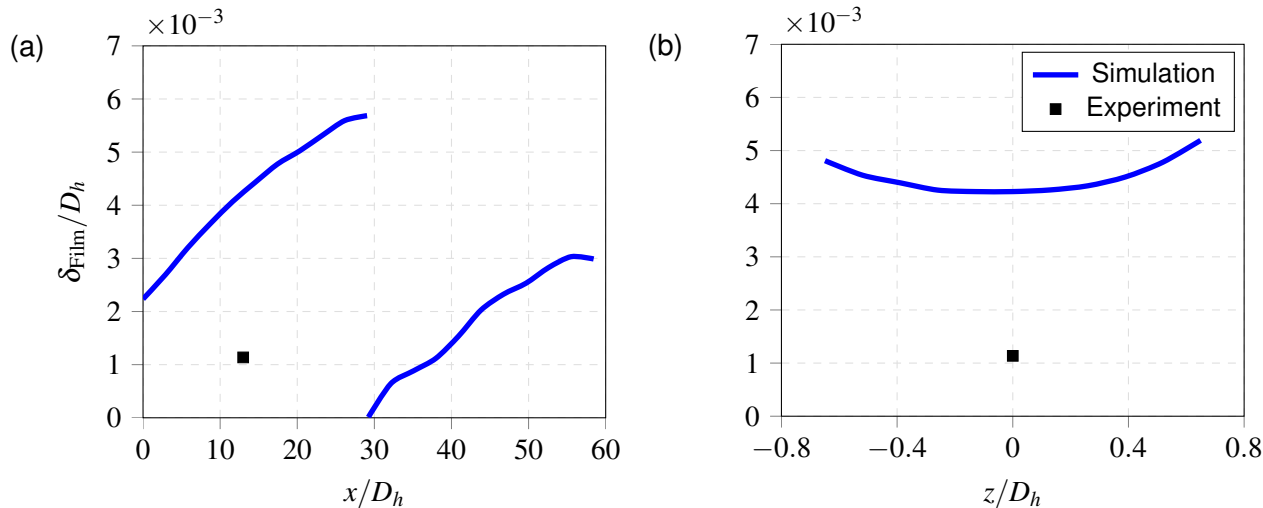


Figure 10 – Distribution of dimensionless film thickness along the channel length (a) and width (b).

film thickness and numerically obtained data. To determine the exact cause of this deviation, further experiments investigating of the film thickness at different positions are required. One possible explanation for this deviation could be attributed to the Bai-Gosman wall-impingement model [10], which needs to be validated for the observed channel flow in this study. Since the film exhibits waviness, it is possible that in the experiments a minimum film thickness is measured at this specific position. Additionally, the wavy film may result in droplet ejection from the film surface into the core flow, leading to film thinning. This effect can be accounted for in STAR-CCM+ using the wave stripping model. The implications of the wave stripping model will be discussed later in this section.

In addition to pressure losses, the amount of separated water through the drainage module (DR2) is essential. As depicted in Figure 1 (a), the injected water can exit the system through two drains and an outlet. One drain (DR1) is located in the humidifier, and another one is situated in the test section (DR2). Each drain is connected to a container placed on a scale to measure the water mass flow rate through the drain. In the experiment, the water mass flow through the drains is calculated from the measured weight on the scale. In unsteady simulations, directly averaging mass flow rates can be challenging and may result in misleading results. Therefore, a mass based averaging was applied for the calculation of the existing dimensionless water mass flow as follow

$$\frac{\dot{m}_{\rm w}}{\dot{m}_{\rm w,inj}} = \frac{\sum_{i=1}^{n} \dot{m}_{\rm w,i} \Delta t_{i}}{(\sum_{i=1}^{n} \dot{m}_{\rm w,inj} \Delta t_{i}) - m_{\rm w,sys}}.$$
(13)

The total water mass exiting through a boundary is summed up for each time step and divided by the

total mass entering the domain minus the water mass in the system at the observed time step. Figure 11 shows the numerically obtained water mass flow rates through drain 1, drain 2 and the outlet, in comparison with experimentally measured data. More than 50% of the injected water exits through the outlet of the test rig. The simulation overestimates the mass flow rate at drain 2 by +14.7% com-

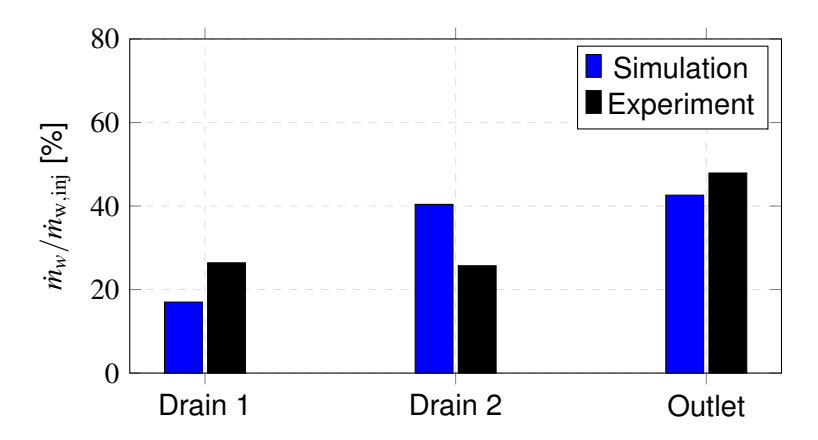


Figure 11 – Comparison of the simulated and measured dimensionless water mass flow through drain 1, drain 2 and outlet.

pared to the measured value in the experiment, see Table 1. One reason for that is the amount of water entering the test section. Since the simulation underestimates the exiting mass flow rate at drain 1 by -9.4% compared to the experiment, more water reaches the test section, resulting in a higher amount of water separation through drain 2. Another reason for this deviation is the larger film thickness values in the simulation compared to the experiment. A thicker film allows for more water separation. As mentioned earlier, the wavy nature of the film can cause liquid mass to be separated

Table 1 – Comparison of experimental and simulation results regarding the influence of the wave stripping model (WS).

	$(\Delta p)_{\mathrm{DR2}}/p_t$ [%]	$\dot{m}_{\mathrm{DR1}}/\dot{m}_{\mathrm{w,inj}}$ [%]	$\dot{m}_{\mathrm{DR2}}/\dot{m}_{\mathrm{w,inj}}$ [%]	$(\delta_{\text{Film}}/D) \times 10^{-3} \text{ [-]}$
Experiment	0.30	26.4	25.7	1.08
no WS	0.20	17.0	40.4	4.26
WS (cH=1)	0.28	16.2	3.7	1.33
WS (cH=4)	0.23	17.4	33.1	4.03

from the film surface due to wave instabilities. Since higher values for the film thickness and for the amount of separated water are obtained in the simulation, compared to the experimental values, the influence of the wave stripping model in STAR-CCM+ is investigated. Different parameters within the wave stripping model can be adjusted for a better agreement with experimental data. One of this parameters is the scale factor of the minimum film thickness (cH), at which film stripping occurs. The influence of two different scaling factors (cH=1, cH=4) on numerical results are listed in Table 1. These results are compared with the initial model, where no wave stripping is considered and with experimental data. The default value (cH=1) within the stripping model leads to an increase of the pressure loss over the drainage module and to a lower value for the film thickness, compared to the initial model, where no stripping is considered. For drain 1, almost the same mass flow rate is obtained, compared to the initial model. Hence, water stripping can be neglected in the humidifier, due to lower air velocities. However, the amount of separated water through drain 2 is significantly reduced, resulting in a deviation of -22% from the experiment. This indicates that a large water mass is ejected from the film into the core flow. This is due to higher air velocities in the test section. In order to reduce the ejected water mass, the scaling factor for the minimum film thickness at which stripping occurs is increased to cH=4. Consequently, wave stripping is considered for higher film thickness values. The numerical results for this scaling factor are shown in the Table 1. The pressure

drop and the separated water mass flow rate through drain 1 remain nearly constant, compared with the values from the initial simulation. However, the mass flow rate through drain 2 deviates yet by +7.4% from the experimental data. The influence of the scaling factor cH is rarely discussed in the literature, where a default value of cH=1 is often chosen [14, 15]. However, the value of the scaling factor cH depends on the specific study and the characteristics of the flow. It can be determined based on numerical data or calibration against experimental results. Hence, further investigations are required for better analysis of this factor. Additionally, edge stripping at the drainage could lead to higher amount of water mass being ejected from the film, resulting in smaller values for the amount of separated water. Since no edge stripping is considered in these simulations, a higher water separation is expected from numerical results.

When a higher number of droplets are injected into the flow, two-way coupling is no longer sufficient. Consequently, interactions between the droplets become crucial, especially in the case of high-density sprays. These interactions include various phenomena, including breakup and collisions. It has been determined that droplet breakup can be neglected due to the lower droplet Weber numbers. However, in a subsequent study, the influence of two different collision models in combination with the wave stripping model (cH=4) is investigated. For both models, the No Time Counter (NTC) collision detection algorithm by Schmidt and Ruthland [16] is used. After the detection of a collision between two droplets, several outcomes may occur depending on the collision Weber numbers. These potential outcomes include bounce, permanent coalescence, reflexive separation, and stretching separation [5]. Empirical regime maps are commonly used to determine the outcomes of collisions between two droplets. The map by O'Rourke [17] and Krajli [18] is such a map. In the latest version of STAR-CCM+ a composite map is implemented to account for bounce, stretching separation and reflexive separation (please refer to STAR-CCM+ User Guide [5]). The numerically obtained results of this investigation are listed and compared to experimental data, as shown in Table 2. Both collision models lead to similar results for pressure loss and film thickness. The film thickness

Table 2 – Comparison of experimental and simulation results regarding the influence of collision models (with cH=4 for WS).

	$(\Delta p)_{\mathrm{DR2}}/p_t$ [%]	$\dot{m}_{\mathrm{DR}1}/\dot{m}_{\mathrm{inj}}$ [%]	$\dot{m}_{\mathrm{DR2}}/\dot{m}_{\mathrm{inj}}$ [%]	$(\delta_{\text{Film}}/D) \times 10^{-3} \text{ [-]}$
Experiment	0.30	26.4	25.7	1.08
NTC (O'Rourke)	0.23	13.3	21.0	3.43
NTC (Composite)	0.23	11.3	26.7	3.63

still significantly differs from the experimentally measured value. Furthermore, both model underestimate the values for the separated amount of water, compared to experimental values. The mass flow rates of the separated water through the drain 1 decrease compared to the initially used model. Regarding the amount of separated water through drain 2, the composite model, with a deviation of  $+1\,\%$  from the experimental data, exhibits better agreement than the model proposed by O'Rourke [17], which deviates by  $-4.7\,\%$  from the experimental data. Except for the film thickness, an overall good agreement is achieved with the experimental data, when the wave stripping model (cH=4) and the composite collision model are considered.

#### 5. Conclusions

Unsteady three dimensional multiphase flow CFD simulations are conducted for a supersaturated channel flow. The numerically obtained values for pressure, film thickness and the amount of separated water are compared with experimentally measured values. Initially, single-phase flow simulations are performed for three different channel designs and two different Mach numbers. Hereby, the geometry of the separation lips in the drainage module are varied. An overall good agreement is achieved for the static pressure, with a maximum deviation below 1%, compared to the experiments. The configuration with no inclined separation lips leads to lower pressure losses, compared to the configurations with inclined separation lips. Therefore, this configuration is further investigated in the multiphase simulations. In order to create a supersaturated multiphase flow, a spray nozzle injects water droplets into the channel flow. A boundary condition has to be specified for this spray nozzle. A solid cone injector model with the Euler-Lagrange approach is used to validate the model against experimentally measured data. Compared to the experiment, a higher spray angle is required to match the measured droplet diameter and velocity distributions. This validated solid cone injector model is then used as a boundary condition for the multiphase flow simulations. Additionally, the solution from the single-phase flow is used as an initial condition. The simulation predicts the pressure loss and the amount of separated water in a reasonable manner, while the thickness of the wall film is overestimated. Additionally, the influence of the wave stripping model and two different collision models has been investigated. An adjustment of the parameters within the wave stripping model lead to better results while the composite collision model within STAR-CCM+ improve the results. Further experimental investigations and detailed numerical simulations are required to determine the reasons for the higher deviations in the film thickness.

## Acknowledgements

The authors like to thank MTU Aero Engines for the permission to publish this paper. The research work associated with this publication has been supported by the German Federal Ministry for Economic Affairs and Climate Action under grant number 20M2110A. The funding of the work through the 2nd call of the Federal Aviation Research Program VI (LuFo VI-2), grant project title 'DINA2030plus', is gratefully acknowledged by all authors of the paper. The authors are responsible for the content of this publication.

## **Contact Author Email Address**

In case of questions or discussion topics regarding the presented work, please send a mail to: marwan.khaled@itlr.uni-stuttgart.de.

#### **Copyright Statement**

The authors confirm that they, and/or their company or organization, hold copyright on all of the original material included in this paper. The authors also confirm that they have obtained permission, from the copyright holder of any third party material included in this paper, to publish it as part of their paper. The authors confirm that they give permission, or have obtained permission from the copyright holder of this paper, for the publication and distribution of this paper as part of the ICAS proceedings or as individual off-prints from the proceedings.

#### References

- [1] Kaiser, S., Schmitz, O., Ziegler, P., and Klingels, H. The Water-Enhanced Turbofan as Enabler for Climate-Neutral Aviation. *Applied Sciences*, 12(23), 12431, 2022.
- [2] Grewe, V., Dahlmann, K., Flink, J., Frömming, C., Ghosh, R., Gierens, K., Heller, R., Hendricks, J., Jöckel, P., Kaufmann, S., Kölker, K., Linke, F., Luchkova, T., Lührs, B., Van Manen, J., Matthes, S., Minikin, A., Niklaß, M., Plohr, M., Righi, M., Rosanka, S., Schmitt, A., Schumann, U., Terekhov, I., Unterstrasser, S., Vázquez-Navarro, M., Voigt, C., Wicke, K., Yamashita, H., Zahn, and A., Ziereis, H. Mitigating the climate impact from aviation: Achievements and results of the DLR WeCare project. Aerospace, 4(3), 34, 2017.
- [3] Cheng, D. Y. Parallel-compound dual-fluid heat engine. U.S. Patent No. 3978661, 1976.
- [4] Revell, A.J., Benhamadouche, S., Craft, T. Laurence, D. A stress-strain lag eddy viscosity model for unsteady mean flow. *International Journal of Heat and Fluid Flow*, 27 (5), pp. 821-830, 2006.
- [5] Siemens P. Simcenter STAR-CCM+ User Guide V18.06. Siemens PLM, 2023. .
- [6] Schiller, L., and Naumann, A. Ueber die grundlegenden Berechnungen bei der Schwerkraftaufbereitung (in German), *Zeitschrift des Vereines Deutscher Ingenieure*, 77(12), pp. 318–320, 1933.
- [7] Sommerfeld, M., van Wachem, B., Oliemans, R. Best Practice Guidelines for Computational Fluid Dynamics of Dispersed Multi-Phase Flows. *European Research Community on Flow, Turbulence and Combustion (ERCOFTAC)*, 1<sup>th</sup> edition, 2008.
- [8] Meredith, K. V., Heather, A., De Vries, J., and Xin, Y. A numerical model for partially-wetted flow of thin liquid films. *Computational Methods in Multiphase Flow VI*, 70: 239, 2011.
- [9] Kistler, S. F.: Hydrodynamics of wetting. Wettability 6, 311-430, 1993
- [10] Bai, C., and Gosman, A.D. Development of methodology for spray impingement simulation. *SAE Technical Paper Series* 950283, 1995.
- [11] Maroteaux, F., Llory, D., Le Coz, J-F., Habchi, C. Liquid film atomization on wall edges separation criterion and droplets formation model. *ASME. J. Fluids Engineering*, 124(3), pp. 565-575, 2002.
- [12] Friedrich, M. A., Lan, H., Drallmeier, J. A., Armaly, B. F. A separation criterion with experimental validation for shear-driven films in separated flows. *ASME. J. Fluids Engineering*, 130(5), 051301, 2008.
- [13] Badra, J. A.; SIM, J., Elwardany, A., Jaasim, M., Violet, Y., Chang, J., Amer, A., Im, H. G. Numerical simulations of hollow-cone injection and gasoline compression ignition combustion with naphtha fuels. *Journal of Energy Resources Technology* 138.5, S. 052202, 2016.
- [14] Zhao, B., Bi, H., Wang, H., Zhou, Y. Experimental and numerical investigation on frosting of finned-tube heat exchanger considering droplet impingement. *Applied Thermal Engineering*, 216, 119134, 2022.
- [15] Skarysz, M., Garmory, A., Escobar, J., Jilesen, J., Gaylard, A. Investigation of wave stripping models on a generic wing-mirror using a coupled level-set volume of fluid simulation. *SAE International Journal of Advances and Current Practices in Mobility*, 2(3):1497-1506, 2020.
- [16] Schmidt, D.P., and Rutland, C.J. A New Droplet Collision Algorithm. *Journal of Computational Physics*, 164, pp. 62–80, 2000.
- [17] O'Rourke, P.J., and Bracco, F. Modeling of Drop Interactions in Thick Sprays and a Comparison with Experiments. *Proceedings of the Institution of Mechanical Engineers*, 9, pp. 101–106, 1980.
- [18] Kralj, C. Numerical Simulation of Diesel Flow Processes. Ph.D. Thesis, Imperial College, London, 1995.